RESEARCH ARTICLE

LASER & PHOTONICS REVIEWS

www.lpr-journal.org

High-Efficiency Electro-Optic Modulator on Thin-Film Lithium Niobate with High-Permittivity Cladding

*Nuo Chen, Kangping Lou, Yalong Yu, Xuanjian He, and Tao Chu**

Thin-film lithium niobate is a promising platform owing to its large electro-optic (EO) coefficients and low propagation loss. However, the large footprints of devices limit their application in large-scale integrated optical systems. A crucial challenge is how to maintain the performance advantage given the design space restrictions in this situation. This work proposes and demonstrates a high-efficiency lithium niobate EO modulator with high-permittivity cladding to improve the electric field strength in waveguides and its overlap with optical fields while maintaining low optical loss and broad bandwidth. The proposed modulator exhibits considerable improvement, featuring a low half-wave voltage–length product of 1.41 V•cm, a low excess loss of ≈0.5 dB, and a broad 3 dB EO bandwidth of >67 GHz. Among all the Mach-Zehnder interferometer modulators reported thus far, the proposed modulator demonstrates notably high modulation efficiency while maintaining excellent high-frequency performance. The design scheme of using high-permittivity cladding may provide a promising solution for improving the integration of photonic devices on the thin-film lithium niobate platform, and these devices may serve as fundamental components in large-scale photonic integrated circuits in the future.

1. Introduction

Lithium niobate ($LiNbO_3$, LN) has been acknowledged as a dominant photonic material owing to its superior and versatile properties, such as a wide transparency window (≈0.35–5 µm) and strong electro-optic (γ_{33}=31pm/V), ferroelectric, and piezoelectric coefficients.[1–3] In recent decades, there has been an increasing need for photonic integrated circuits to have lower power consumption and device footprints due to the increasing complexity of optical systems. The availability of wafer-scale and high-quality thin-film lithium niobate (TFLN) on insulators has garnered widespread interest in integrated optics[4–7] because TFLN not only inherits the excellent physical properties of LN but also achieves stronger optical field confinement and improves the element integration density.[8–10]

As crucial components of photonic integrated circuits, EO modulators are widely used in telecommunications, data communications, optical sensors, and quantum optics, among other applications.[11–16] TFLN modulators have experienced rapid development in recent years,[17–22] and numerous high-efficiency modulators have been demonstrated.[23–30]

Liu et al. increased the EO modulation efficiency to a voltage–length product of 1.75 V•cm using a shallowly etched lithium niobate waveguide.[29] Owing to the disparity between the relative permittivities of lithium niobate and silica, the electrical field primarily affected the LN core through the slab. The shallowly etched waveguide increased the proportion of the waveguide slab, enhancing the electric field density. However, the modulation efficiency achievable using this method had an upper limit owing to the restriction of light-propagation loss arising from electrode absorption. Another representative study demonstrated a new electrode extending from the sides to the top of the waveguide, creating a much stronger electric field within the narrow gap. The modulation efficiency was increased to 1.32 V•cm, the highest on record to date.[30] Nevertheless, this irregular electrode could have a considerable influence on microwave attenuation, with a measured EO bandwidth of ≈3 GHz.

It is evident that the voltage–length product, bandwidth, and optical loss in the aforementioned reports continue to sustain critical trade-offs constrained by light-metal absorption and inefficient microwave signal delivery.[7] How to improve the modulation efficiency while preserving other favorable performance measures remains to be investigated.

This article proposes and demonstrates an LNOI high-efficiency EO modulator with composite cladding. The design using high-permittivity (ε) cladding alters the electric field intensity distribution, which contributes to considerable improvements in the electric field strength in waveguides and enhances the overlap between the electric and optical fields. Additionally, the devices preserve low optical loss and high bandwidth simultaneously. That is, the proposed solution goes beyond the above constraints, introducing new variables to improve efficiency without affecting other performance measures. The proposed modulator exhibited a low excess loss of ≈0.5 dB and a low voltage-length product of 1.41 V•cm. The 3 dB EO bandwidth of the modulator was measured to be greater than 67 GHz. This work provides a general solution for improving the integration of photonic devices on the TFLN platform with high-ε cladding.

N. Chen, K. Lou, Y. Yu, X. He, T. Chu
College of Information Science and Electronic Engineering
Zhejiang University
Hangzhou 310027, China
E-mail: chutao@zju.edu.cn

DOI: 10.1002/lpor.202200927

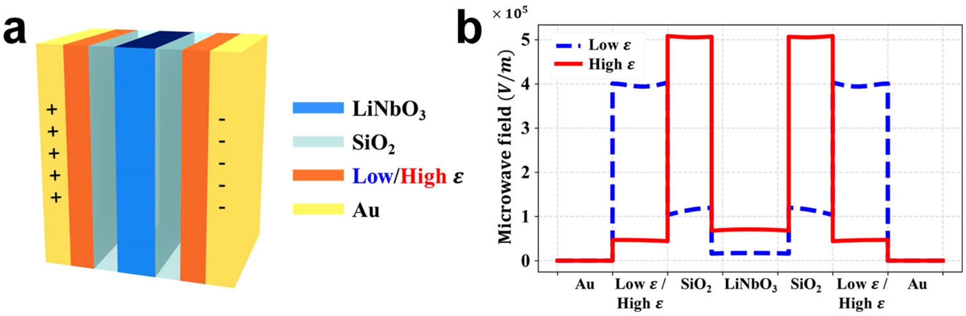

Figure 1. a) Schematic diagram of the parallel plates. b) Simulated microwave field distribution of electrode plates for low-ε (blue line) and high-ε (red line) media. The electric field inside LN has been increased by more than four times.

2. Result and Discussion

2.1. Principle and Design

The complicated electric field distribution inside the phase shifter of the modulator is simplified to the electric field issue inside the parallel plate capacitor, as shown in **Figure 1**a. A parallel dielectric capacitor consists of two parallel metallic conducting plates with a dielectric medium, silicon dioxide (SiO_2), and LN filled in between. In this article, we categorize materials with a relative permittivity equal to or less than that of SiO_2 as low-ε dielectrics, such as air. Conversely, materials with a relative permittivity greater than that of SiO_2 are classified as high-ε materials, exemplified by Si_3N_4 ($\varepsilon \sim 11.1$) and glycerol ($\varepsilon \sim 44$).

According to Gauss's law, at the interface of a medium with different ε, the electric field strength satisfies Maxwell's equation:

$$D = \varepsilon_1 E_1 = \varepsilon_2 E_2 \tag{1}$$

Substituting into the interior of the electrode plates yields

$$\varepsilon E = \varepsilon_{SiO_2} E_{SiO_2} = \varepsilon_{LN} E_{LN} \tag{2}$$

where ε, ε_{SiO_2}, and ε_{LN} denote the relative permittivities of the medium, SiO_2, and LN, respectively, and E, E_{SiO_2}, and E_{LN} denote the electric field strengths within them. The electric field strength inside LN can be improved by replacing the external medium with a larger relative permittivity. Low and high ε values of $\approx$1 and 44, respectively, are substituted into the calculation, and the electric field distribution diagram inside the electrode plate is shown in Figure 1b. The electric field inside LN has been increased by more than four times.

We introduced this idea to the modulator, whose structure is shown in **Figure 2**. It is designed on an LNOI wafer with a 600-nm-thick X-cut LN layer and a 4.7-µm-thick SiO_2 layer. The Mach–Zehnder interferometer (MZI) modulator consists of waveguide phase shifters and multimode interferometers. Gold traveling-wave electrodes are laterally spaced in a ground–signal–ground configuration. The composite claddings consist of a SiO_2 layer and an upper high-ε material layer, hereinafter referred to as the upper cladding, as depicted in Figure 2b. The basic structural parameters are the waveguide width (w), ridge etching depth (d), gap between the signal and ground electrode (gap), and width of the SiO_2 cladding (w_{SiO_2}). A cross-sectional view of the modulator with fabrication parameters is shown in Figure 2c.

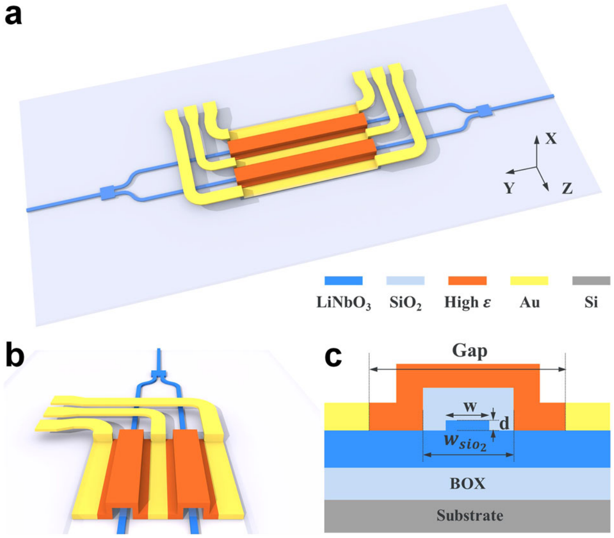

Figure 2. a) 3D schematic of the LNOI modulator. b) Perspective view of the modulator phase shifter. c) Cross-sectional view of the modulator with the fabrication parameters.

2.2. Simulation Results

Previous studies have primarily employed two common design approaches: one with the gap between electrodes and waveguide fully exposed to air,[18] and the other with the gap entirely covered by SiO_2 ($\varepsilon \sim 3.9$).[7] These two structures can be categorized as a type of configuration that involves a cladding with a low relative permittivity. We simulated the microwave field distribution of a phase shifter with the low-ε cladding, high-ε cladding, and composite cladding, as shown in **Figure 3**. To make the comparison of the simulation results more obvious, we used air as the low-ε cladding and glycerol as the high-ε cladding. For the modulator with the low-ε cladding, there is a huge difference in relative permittivity between the cladding and the LN ($\varepsilon \sim 28$) ridge waveguide. Due to the sudden change of the relative permittivity at the interface, the electric field strength is discontinuous at the dielectric level, the ratio being inversely proportional to the

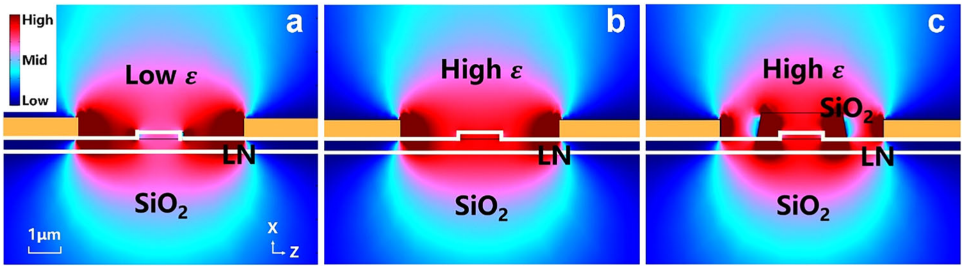

Figure 3. Cross-sectional views of simulated z-component of the microwave field distribution of TFLN modulator phase shifter with a) the low-ε cladding, b) high-ε cladding, and c) composite cladding.

relative permittivity of the medium. That is, the electric field is concentrated in the air. However, the electric field strength in the waveguides—which is effective for modulation—is limited.

For the modulator with the pure high-ε cladding, because the relative permittivity of glycerol is larger than that of the air or SiO_2, the electric field strength inside the LN waveguide is higher than that of the LN waveguide with conventional SiO_2 cladding.

For the modulator with the composite cladding, because the relative permittivity of glycerol is larger than that of SiO_2, the electric field strength inside the glycerol cladding layer is lower, whereas the electric field strength in the SiO_2 cladding layer and the LN ridge waveguides is higher than that of the LN waveguide with conventional SiO_2 cladding. Meanwhile, because the electric field distribution inside the LN is continuous, the electric field within the waveguide rises steeply—from low to high—near the interface of the composite dielectric cladding, manifesting as a new electric field intensity peak. The electric field strength in the slab near the ridge waveguide area also increases. Overall, with the combined effect of these two attributes, the electric field strength in LN waveguides is substantially enhanced compared to that of the modulator with the conventional SiO_2 cladding and close to that of the modulator with the pure high-ε cladding.

However, glycerol, as mentioned above, stands as a special case due to its exceptionally high dielectric constant and very low refractive index of ≈1.48. By contrast, most high-ε materials typically exhibit high refractive indices, such as Si_3N_4, which possesses a high refractive index of ≈1.97. Consequently, these materials have the potential to weaken the optical confinement and reduce the overlap between the electrical and optical fields (Γ), ultimately leading to a decrease in the electro-optic efficiency. Therefore, we have retained the SiO_2 cladding to maintain a high-index contrast of >0.7 near the ridge waveguide. This ensures strong field confinement and subsequently reduces scattering losses. To analyze the optical mode profiles and calculate the waveguide transmission loss, we employed the FDE module in Lumerical Mode software. The simulation compared the optical mode profiles of two structures: one completely covered by high-ε cladding (Si_3N_4) and the other with SiO_2 cladding. The simulated optical mode profile for the transverse electric (TE) mode is presented in **Figure 4**. Evidently, the presence of SiO_2 cladding restricts the optical mode field effectively and mitigates light propagation loss arising from electrode absorption, reducing the loss from 137.4 dB cm^{-1} to 13.8 dB cm^{-1}. This allows integration of various high-ε materials in the modulator without causing a detrimental increase in loss. Consequently, the proposed structure exhibits enhanced versatility and practicality.

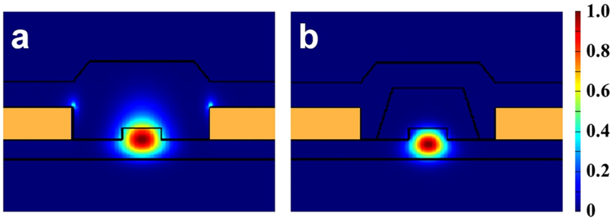

Figure 4. Simulated TE optical mode profiles of phase shifter with a) high-ε cladding, and b) composite cladding.

To verify this idea, we used COMSOL Multiphysics and Lumerical Mode software to conduct a co-simulation, considering the effects of the electric and optical field distributions on the modulation efficiency. We simulated the effects of different materials on the modulation efficiency with the same structural parameters. The waveguides featured a top width of w = 1.4 µm and ridge etching depth of d = 200 nm. The gap between the signal and ground electrode gap was set to 5 µm, and the width of the SiO_2 cladding (w_{SiO_2}) was set to 3.2 µm. **Figure 5**a shows that the modulation efficiency increases as the relative permittivity of the upper cladding increases. For the modulators without upper cladding and with glycerol upper cladding, the modulation efficiency increases from 1.95 to 1.56 V•cm, illustrating that composite cladding causes a marked improvement in modulation efficiency.

To investigate the performance of the proposed design further, we introduced structural variations based on different materials. We used $P = \frac{gap - w_{SiO_2}}{gap - w}$ to describe the proportion of the upper cladding and to analyze the effects of P on the modulation efficiency with various materials when the electrode gap (gap) was a constant, as shown in Figure 5b. When the proportion of the upper cladding increases, the modulator is more linearly efficient. Moreover, when the modulator is almost entirely covered with glycerol, the modulation efficiency is 1.37 V•cm. Air is the only counterexample, as it has a relative permittivity lower than that of SiO_2.

To analyze the impact of glycerol on the traveling-wave electrodes, we conducted simulations using the HFSS software. The simulations involved comparing the electrodes with and without glycerol coverage. We analyzed three key indicators: the frequency-dependent characteristic impedance Z, the RF

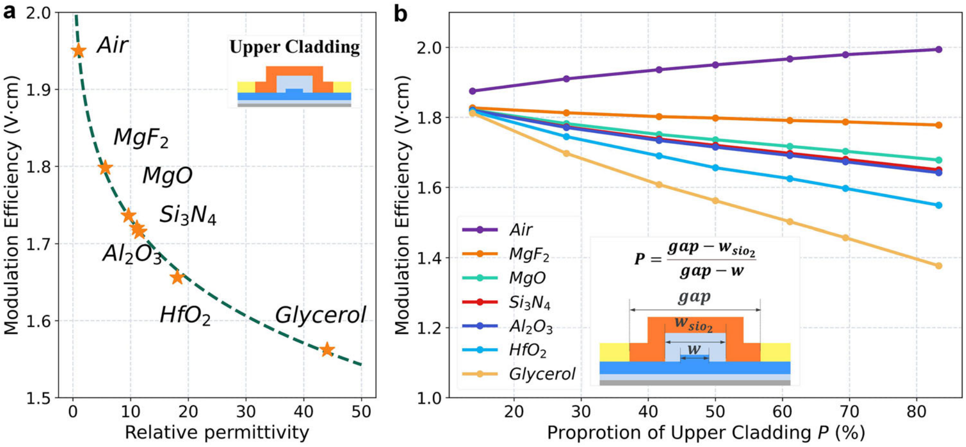

Figure 5. a) Simulated modulation efficiencies of modulators with different materials as the upper cladding. b) Simulated modulator efficiencies with different upper claddings versus the proportion of the upper cladding. The inset shows the specific structure with the fabrication parameters.

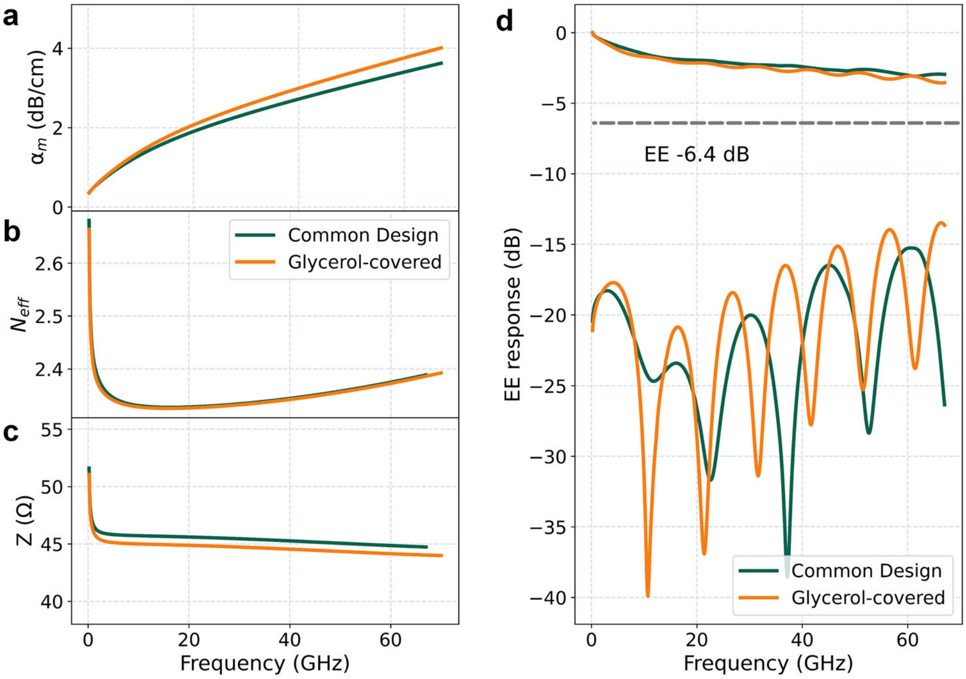

Figure 6. Simulation of a) RF loss coefficient α_m, b) RF effective index n_{eff}, and c) characteristic impedance Z as a function of frequency for modulators covered with and without glycerol. d) Simulation of EE reflection S11 and EE transmission S12 for devices with and without glycerol coverage.

effective index n_{eff}, and the RF loss coefficient α_m, as depicted in Figure 6a–c. It should be noted that these curves exhibit a high degree of similarity, indicating that the presence of glycerol does not significantly impair the high-frequency performance of the electrodes. Impedance matching is ensured as the value of Z remains ≈45 Ω over the RF spectrum. The RF effective index n_{eff} is ≈2.35, which closely aligns with the optical group index of 2.3, thus resulting in velocity matching for this modulator. The RF loss coefficient α_m exhibits a relatively low value of 0.507 dB·cm^{-1}·GHz$^{-1/2}$ with glycerol coverage and 0.474 dB·cm^{-1}·GHz$^{-1/2}$ without glycerol coverage. Furthermore, we have included the simulation results of the electrical-electrical (EE) responses, as illustrated in Figure 6d. It is evident from the data that the S21 response of the devices, irrespective of glycerol coverage, exhibits a striking resemblance, except for the presence of resonances at specific frequencies.

3. Measurement Results for the Fabricated Device

The proposed LNOI modulators were fabricated on an LNOI wafer from NANOLN using a 600-nm-thick X-cut TFLN layer and a 4.7-µm-thick buried SiO$_2$ layer. The pattern was defined using an i-line stepper, and a 200-nm thick LN layer was etched using inductively coupled plasma (ICP) reactive-ion etching. Subsequently, an 800-nm thick SiO$_2$ layer was deposited on the top of the waveguides using plasma-enhanced chemical vapor

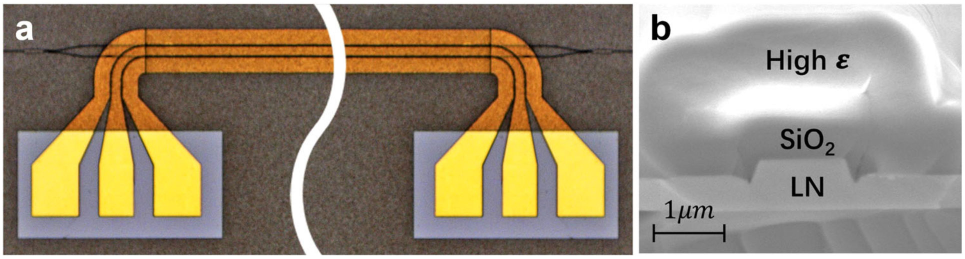

Figure 7. a) Microscope image of the fabricated LNOI modulator. b) SEM image of the cross-sectional view of the modulator phase shifter.

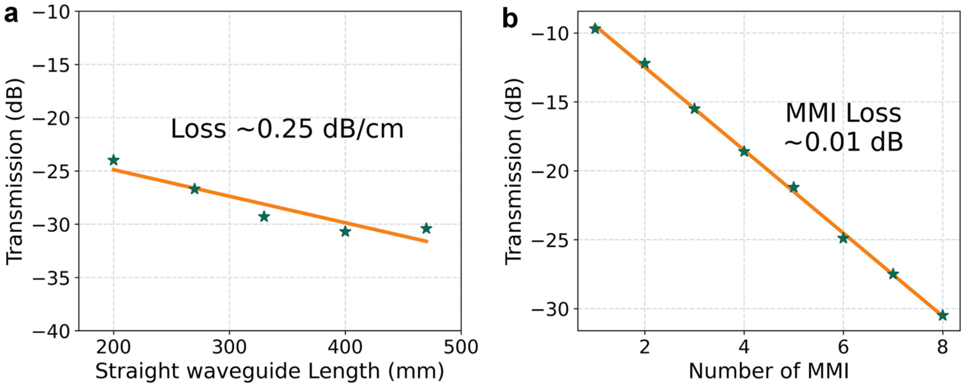

Figure 8. Measured loss of a) the straight waveguide and b) 1 × 2 multimode interferometers.

deposition and etched using ICP. A 600-nm-thick Ti/Au layer was subsequently deposited via electron-beam evaporation and lift-off to form the electrodes.

For materials such as MgF$_2$, MgO, and Al$_2$O$_3$, a 500-nm-thick high-ε material layer was deposited using electron-beam evaporation. Subsequently, the pattern was defined on the deposited layer using photolithography, followed by the implementation of dry etching to selectively remove a specific section of the layer. This process generates the necessary space for the subsequent placement of the probe. **Figure 7** shows microscope and scanning electron microscope (SEM) images of the fabricated device. Regarding glycerol, we actually fabricated glycerol-coated devices, as depicted in **Figure 9**a. Because glycerol is a liquid at room temperature, we applied a drop of glycerol directly to the modulation area of the device.

To determine the on-chip losses of our modulator, we designed a direct waveguide on the same chip with the same cladding and of the same length as the modulator. By subtracting the fiber-to-fiber insertion losses of the two waveguides, we could easily obtain the on-chip losses specific to our modulator. Furthermore, we conducted additional measurements to calibrate the loss of the waveguide and the 1 × 2 MMI structure to validate the low-loss characteristics of our device. To obtain accurate test results, we fabricated a series of folded waveguides and employed the cut-back method[31] to measure the waveguide propagation loss. All the experiments mentioned in this paper were conducted at a wavelength of 1550 nm. Our measurements indicated a transmission loss of ≈0.25 dB cm^{-1} for the straight waveguide, as illustrated in Figure 8a. Similarly, by performing cascade tests, we recorded an additional loss of 0.01 dB for the 1 × 2 MMI structure, as shown in Figure 8b (details can be found in Supporting Information). The fiber-to-fiber loss of the straight waveguide was measured to be 6.7 dB. Given that the total length of our chip is 0.6 cm, the on-chip loss of the straight waveguide is negligible, while the fiber-to-chip interface loss equates to ≈3.3 dB facet^{-1}. Comparatively, the fiber-to-fiber loss of the modulator is 7.2 dB, resulting in an on-chip loss of 0.5 dB.

We characterized the modulation efficiency of the fabricated LNOI modulator using the experimental setup shown in Figure 9b. Light from a tunable laser at 1550 nm (SANTEC TSL-550) was amplified using an erbium-doped fiber amplifier (EDFA: Keopsys CEFA-C-PB) and subsequently launched into the device under test. A polarization controller was used to adjust the input light to TE mode. Subsequently, the modulated light was detected using a high-speed photodetector. An arbitrary signal generator (AWG: GW Instek AFG-3051) was employed to provide a 1 MHz triangular voltage sweep. A real-time oscilloscope was used to measure the signal from the AWG and the photodetector (PD: Light sensing LSIHPD-A12). To quantify the system loss, reference waveguides were attached to the chip. As a result, the fiber–waveguide coupling loss and straight waveguide loss could be filtered to derive the normalized on-chip insertion loss of the device.

More than five materials were utilized as the upper cladding to confirm the reliability and universality of our study. However, owing to process limitations, some cladding films fractured, resulting in vacant data. **Figure 9**d shows the EO half-wave voltage measurement for the 4-mm-long devices with different materials

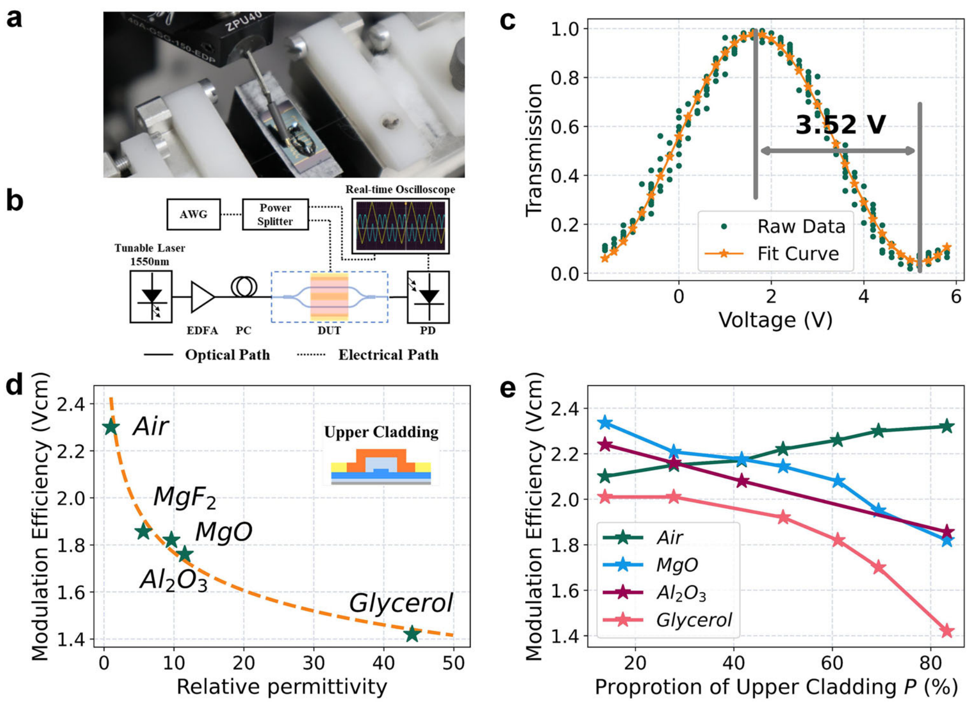

Figure 9. a) Microscope image of the device under test. b) Setup for modulation efficiency measurement. c) Normalized optical transmission as a function of applied voltage for the 4-mm device covered with glycerol, showing a Vπ of 3.52 V and VπL of 1.41 V•cm. d) Measured modulation efficiencies of modulators with different materials as the upper cladding. e) Measured modulation efficiencies of modulators with different materials as the upper cladding versus the proportion of the upper cladding.

as the upper cladding when the width of the SiO$_2$ cladding w_{SiO_2} = 3.2 µm. The experimental results agree well with the simulation results.

The modulation efficiency increases as the relative permittivity of the upper cladding increases. Figure 9e shows the influence of the proportion of the upper cladding on the modulation efficiency. The experimental results follow the rule that when the proportion of the upper cladding increases, the modulator becomes more efficient. We found the measured modulation efficiency using high-refractive-index cladding to be worse than that in the simulation, which may be due to the weak optical confinement and the deterioration of the overlap factor being more

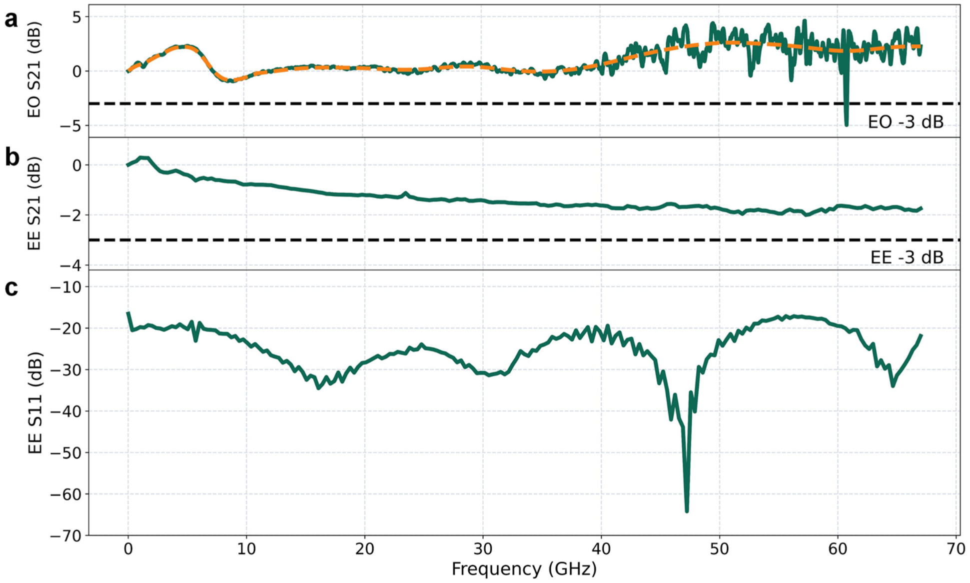

Figure 10. Measured a) EO S21, b) EE reflection S11, and c) EE transmission S21 for the 4-mm long device covered with glycerol.

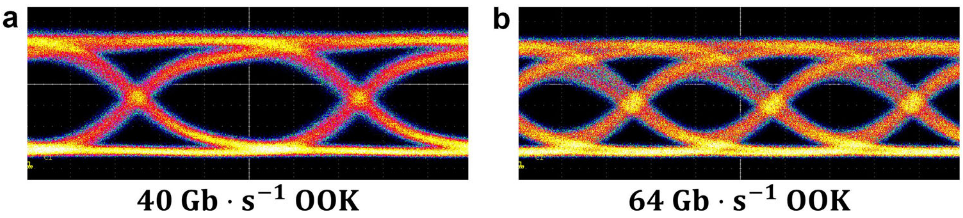

$40\ \mathbf{Gb \cdot s^{-1}}$ **OOK**

$64\ \mathbf{Gb \cdot s^{-1}}$ **OOK**

Figure 11. Measured optical eye diagrams at data rates of a) 40 Gb s^{-1} and b) 64 Gb s^{-1} OOK.

than expected. When $P \approx 85\%$, there is a reverse-trend data point, which could be a result of an overlay error—the finer the structure, the more it is affected. The impact of the upper cladding leads to more light leakage, which influences the modulation efficiency.

Overall, there is good agreement between the simulated and measured data, proving that the simulation offers useful guidance for improving modulator performance. Glycerol is the most suitable cladding material, satisfying the need for both a low refractive index and a high relative permittivity. When the modulator is almost entirely covered with glycerol, the measured Vπ is 3.52 V in a push-pull configuration, as depicted in Figure 9c, and the corresponding voltage–length product (VπL) is 1.41 V•cm.

Additionally, we performed characterizations of the EE responses and EO responses, as depicted in **Figure 10**. The device shows a 3-dB EO bandwidth of over 67 GHz. The observed peak below 10 GHz in the response may be caused by the impedance mismatch, which may be attributed to the fact that the electrode impedance is lower than the 50 Ω load. However, the response beyond 40 GHz exhibits a jagged and upward trend, which may be attributed to system noise. The measured EE transmission, represented by S21, exhibits an ultra-low roll-off of <2 dB at 67 GHz for the 4-mm long devices. Furthermore, the EE reflection, denoted as S11, consistently maintains a level below −16.5 dB across the entire frequency range that was measured. A slight deviation exists between the measured and simulated results. We attribute this disparity to subtle differences that may arise between the actual devices manufactured and the simulation models utilized.

Subsequently, we proceeded to evaluate the performance of the 4-mm long device in terms of high-speed data transmissions. **Figure 11** illustrates the eye diagrams of the transmitted signals utilizing 40 Gb s^{-1} on–off keying (OOK) and 64 Gb s^{-1} OOK, both of which exhibit a significantly spacious eye-opening. The extinction ratios for these configurations were measured at 9.3 and 7.8 dB, respectively.

The performances of the reported LNOI MZI modulators are summarized in **Table 1**. Among these modulators, our modulator fabricated via standard photolithography shows the lowest voltage-length products and the lowest optical loss, while having no impact on the device's high-frequency performance. In brief, the modulator developed in this study achieved a satisfactory compromise among modulation efficiency, loss, and bandwidth.

Table 1. Performance comparison of the reported LNOI MZI modulators.

Reference	Device length [mm]	$V_\pi \cdot L(V \cdot cm)$	Loss [dB]	3 dB EO bandwidth [GHz]
[7]	5	2.2	0.5	100 GHz
[20]	4	2.5	–	100 GHz
[21]	5	3.3	–	170 GHz
[22]	5	2.5	2.5	70 GHz
[29]	5	1.75	2.5	>40 GHz
[30]	7.5	1.32	2	>3 GHz
This Work	4	1.41	0.5	>67 GHz

4. Conclusions

We experimentally demonstrated an LNOI high-efficiency EO modulator with composite cladding. The structure of the composite cladding could increase the electric field strength in the LNOI waveguide, thereby improving the modulation efficiency without negatively impacting the high-frequency performance. The measured voltage–length product was 1.41 V•cm when using glycerol cladding. This approach is a novel method of improving the modulation efficiency based on the traditional MZI modulator structure, which could be combined with other structures to achieve better performance. Our suggested design strategy of using high-permittivity cladding may provide a means of enhancing photonic device integration on the TFLN platform and function as a key element in future large-scale photonic integrated circuits.

Supporting Information

Supporting Information is available from the Wiley Online Library or from the author.

Acknowledgements

This work was supported by the National Key R&D Program of China (2019YFB2203702). The authors thank Huawei for instrumental support and expert technical assistance. The authors acknowledge Zhejiang University Micro and Nano Processing Platform for providing the facility support. The authors thank Mrs. Qingjiao Mi for assistance with the experiments.

Conflict of Interest

The authors declare no conflict of interest.

Data Availability Statement

The data that support the findings of this study are available from the corresponding author upon reasonable request.

Keywords

electro-optic modulators, integrated optics, lithium niobate on insulators (LNOI), high modulation efficiency

Received: December 1, 2022
Revised: July 25, 2023

---

[1] D. Zhu, L. Shao, M. Yu, R. Cheng, B. Desiatov, C. J. Xin, Y. Hu, J. Holzgrafe, S. Ghosh, A. Shams-Ansari, E. Puma, N. Sinclair, C. Reimer, M. Zhang, M. Lončar, *Adv. Opt. Photonics* **2021**, *13*, 242.
[2] D. Janner, D. Tulli, M. Garc ́ıa-Granda, M. Belmonte, V. Pruneri, *Laser Photonics Rev.* **2009**, *3*, 301.
[3] R. S. Weis, T. K. Gaylord, *Appl. Phys. A* **1985**, *37*, 191.
[4] A. Boes, B. Corcoran, L. Chang, J. Bowers, A. Mitchell, *Laser Photonics Rev.* **2018**, *12*, 1700256.
[5] A. Honardoost, K. Abdelsalam, S. Fathpour, *Laser Photonics Rev.* **2020**, *14*, 2000088.
[6] M. Zhang, C. Wang, P. Kharel, D. Zhu, M. Lončar, *Optica* **2021**, *8*, 652.
[7] C. Wang, M. Zhang, X. Chen, M. Bertrand, A. Shams-Ansari, S. Chandrasekhar, P. Winzer, M. Loncar, *Nature* **2018**, *562*, 101.
[8] Y. Qi, Y. Li, *Nanophotonics* **2020**, *9*, 1287.
[9] X. Liu, B. Xiong, C. Sun, J. Wang, Z. Hao, L. Wang, Y. Han, H. Li, Y. Luo, *Opt. Express* **2021**, *29*, 41798.
[10] G. Chen, N. Li, J. D. Ng, H.-L. Lin, Y. Zhou, Y. H. Fu, L. Y. T. Lee, Y. Yu, A.-Q. Liu, A. J. Danner, *Adv. Photonics* **2022**, *4*, 034003.
[11] G. Sinatkas, T. Christopoulos, O. Tsilipakos, E. E. Kriezis, *J. Appl. Phys.* **2021**, *130*, 101901.
[12] P. J. Winzer, D. T. Neilson, A. R. Chraplyvy, *Opt Express* **2018**, *26*, 24190.
[13] R. Stabile, A. Albores-Mejia, A. Rohit, K. A. Williams, *Microsyst. Nanoeng* **2016**, *2*, 15042.
[14] J. P. Höpker, T. Gerrits, A. Lita, S. Krapick, H. Herrmann, R. Ricken, V. Quiring, R. Mirin, S. W. Nam, C. Silberhorn, T. J. Bartley, *APL Photonics* **2019**, *4*, 056103.
[15] X. Qiang, Y. Wang, S. Xue, R. Ge, J. Wu, *Sci. Adv.* **2021**, *7*, eabb8375.
[16] E. L. Wooten, K. M. Kissa, A. Yi-Yan, E. J. Murphy, D. A. Lafaw, P. F. Hallemeier, D. E. Bossi, *IEEE J. Sel. Top. Quantum Electron.* **2000**, *6*, 69.
[17] B. Desiatov, A. Shams-Ansari, M. Zhang, C. Wang, M. Lončar, *Optica* **2019**, *6*, 380.
[18] A. J. Mercante, S. Y. Shi, P. Yao, L. L. Xie, R. M. Weikle, D. W. Prather, *Opt. Express* **2018**, *26*, 14810.
[19] R. Safian, M. Teng, L. Zhuang, S. Chakravarty, *Opt. Express* **2020**, *28*, 25843.
[20] F. Valdez, V. Mere, N. Boynton, T. A. Friedmann, S. Arterburn, C. Dallo, A. T. Pomerene, A. L. Starbuck, D. C. Trotter, A. L. Lentine, A. Kodigala, S. Mookherjea, *IEEE Photon. Technol. Lett.* **2023**, *35*, 633.
[21] F. Arab Juneghani, M. Gholipour Vazimali, J. Zhao, X. Chen, S. T. Le, H. Chen, E. Ordouie, N. K. Fontaine, S. Fathpour, *Adv. Photonics Res.* **2023**, *4*, 2200216.
[22] M. He, M. Xu, Y. Ren, J. Jian, Z. Ruan, Y. Xu, S. Gao, S. Sun, X. Wen, L. Zhou, L. Liu, C. Guo, H. Chen, S. Yu, L. Liu, X. Cai, *Nat. Photonics* **2019**, *13*, 359.
[23] A. N. R. Ahmed, S. Nelan, S. Shi, P. Yao, A. Mercante, D. W. Prather, *Opt. Lett* **2020**, *45*, 1112.
[24] D. Mao, C. Cheng, F. F. Wang, Y. H. Xiao, T. T. Li, L. Chang, A. Soman, T. Kananen, X. Zhang, M. Krainak, P. Dong, T. Y. Gu, *IEEE J. Sel. Top. Quant.* **2021**, *2*, 27.
[25] B. C. Pan, H. Y. Cao, Y. S. Huang, Z. Wang, K. X. Chen, H. Li, Z. J. Yu, D. X. Dai, *Photonics Res* **2022**, *10*, 697.
[26] J. Jian, M. Xu, L. Liu, Y. Luo, J. Zhang, L. Liu, L. Zhou, H. Chen, S. Yu, X. Cai, *Opt. Express* **2019**, *27*, 18731.
[27] P. A. Stockton, K. A. Wernsing, J. J. Field, J. Squier, R. A. Bartels, *APL Photonics* **2019**, *4*, 100802.
[28] X. Huang, Y. Liu, Z. Li, H. Guan, Q. Wie, M. Tan, Z. Li, *Opt. Lett.* **2021**, *46*, 2811.
[29] Y. Liu, H. Li, J. Liu, S. Tan, Q. Lu, W. Guo, *Opt. Express* **2021**, *29*, 6320.
[30] M. W. Jin, J. Y. Chen, Y. M. Sua, P. Kumar, Y. P. Huang, *Opt. Lett.* **2021**, *46*, 1884.
[31] A. Peczek, C. Mai, G. Winzer, L. Zimmermann, in *IEEE 33rd International Conference on Microelectronic Test Structures (ICMTS)*, Edinburgh, UK **2020**.
[32] M. Xu, M. He, H. Zhang, J. Jian, Y. Pan, X. Liu, L. Chen, X. Meng, H. Chen, Z. Li, X. Xiao, S. Yu, S. Yu, X. Cai, *Nat. Commun.* **2020**, *11*, 3911.